Croatian Society for Materials Protection

Metalurgija/Metallurgy

Vol. 66 No. 1 / 2026

Heat Treatment Optimization and Corrosion-Wear Mechanism of Sn-Microalloyed Low-Alloy Wear-Resistant Steel for Archery Training Robot

Hongxing Liu [1], Yufang Wei [2] and Shaoyong Yang [3,*]

https://doi.org/10.64486/m.66.1.12

[1] Changsha Normal University, Changsha, Hunan, China; Liuhongxing@csnu.edu.cn
[2] Shaanxi Police College, Xi'an, Shaanxi, China; wyf1431361165@163.com
[3] Huaihua University, Huaihua, Hunan, China; shaoyong@hhtc.edu.cn
* Correspondence: shaoyong@hhtc.edu.cn; Tel.: +8615273286390

Type of the Paper: Article
Received: March 23, 2026
Accepted: July 8, 2026

Abstract: Low-alloy wear-resistant steel is critical for mechanical transmission components serving under reciprocating friction and corrosive environments. To meet the service requirements of core transmission components of archery training robots, two Sn-microalloyed low-alloy wear-resistant steels (0.04 wt.% and 0.20 wt.% Sn) were designed based on commercial NM450 steel in this work. The effects of Sn on the continuous cooling transformation, microstructure evolution, mechanical properties, and corrosion-wear performance of the steels were systematically investigated, and the optimal heat treatment process was determined. The results show that both steels have a critical cooling rate of 20 °C/s for full martensitic structure with excellent hardenability. The optimized heat treatment enables a well-balanced strength, hardness and toughness of the steels. The 0.20 wt.% Sn steel exhibits significantly improved corrosion resistance and corrosion-wear performance, which is attributed to Sn-induced formation of dense and stable rust layer that inhibits corrosion-wear synergy. This study provides theoretical and data support for composition design and heat treatment optimization of low-alloy wear-resistant steel for archery training robots.

Keywords: archery training robot; low-alloy wear-resistant steel; Sn microalloying; heat treatment; corrosion-wear

1. Introduction

Low-alloy wear-resistant steel is widely used in construction machinery, transportation equipment and robot transmission systems due to its high strength, excellent wear resistance and low production cost [1]–[3]. For mechanical transmission components subjected to long-term reciprocating friction and complex corrosive environments, the failure mode is usually the coupled effect of corrosion and wear: the corrosive medium causes electrochemical corrosion of the matrix, and the friction load continuously destroys the corrosion product film, exposing the fresh matrix and accelerating the corrosion process, which in turn aggravates the wear of materials, forming a positive feedback of failure and significantly reducing the service life of components [4], [5]. Therefore, improving the corrosion-wear resistance of low-alloy wear-resistant steel through composition design and heat treatment process optimization has become a key research direction in the field of metallurgical materials.

The performance optimization of low-alloy wear-resistant steel mainly depends on microalloying and heat treatment process regulation. At present, microalloying elements such as Nb, V, Ti and Cr are widely used to improve the hardenability and wear resistance of steel, but the improvement effect on corrosion resistance is limited, and the production cost is high [6]–[8]. Tin (Sn), as a low-cost microalloying element, has attracted extensive attention in recent years. Studies have shown that Sn can form oxides with high chemical stability in steel, optimize the compactness of the rust layer, and significantly improve the corrosion resistance of steel in chloride ion environments [9], [10]. Meanwhile, Sn can regulate the phase transformation behavior of steel during continuous cooling, and affect the microstructure and mechanical properties of the matrix through grain boundary segregation and solid solution strengthening [11], [12]. Shi et al. [13] found that Sn alloying can promote the transformation of metastable γ-FeOOH to stable α-FeOOH in the rust layer of weathering steel, and significantly improve the protective performance of the rust layer. Liu et al. [14] confirmed that the synergistic effect of Sn and Cr can construct a dense inner rust layer barrier, effectively blocking the penetration of chloride ions. However, existing research on Sn microalloying mainly focuses on weathering steel and stainless steel, and the regulation mechanism of Sn on the continuous cooling transformation behavior, heat treatment process adaptability and corrosion-wear performance of low-alloy wear-resistant steel is still unclear, and the optimal process matching between composition design and heat treatment has not been established.

For the corrosion-wear performance of low-alloy wear-resistant steel, extensive prior works have reached a consensus that the wear resistance is predominantly governed by the matrix microstructure characteristics (including phase type, grain size) and macro-hardness, whereas the corrosion resistance is co-determined by the steel's chemical composition and the barrier effect of the surface rust layer [15], [16]. In this field, Zhang et al. [17] systematically evaluated the influence of tempering temperature on the corrosion-wear behavior of low-alloy wear-resistant steel, and demonstrated that tempered sorbite delivers a superior combination of corrosion resistance and wear resistance over full martensite. Liu et al. [18] further uncovered the synergistic mechanism of Cr and Ni in optimizing the corrosion-wear resistance of low-alloy steel in marine environments, and established a quantitative relationship between rust layer protective properties and material loss rate. Despite these advances, the influence of Sn microalloying on the corrosion-wear coupling behavior of low-alloy wear-resistant steel has rarely been systematically investigated, and the intrinsic regulation mechanism of Sn on the corrosion-wear synergy remains unclear. It is worth noting that existing studies [19], [20] have verified the positive effect of Sn on the atmospheric corrosion resistance of low-alloy steel, and clarified the electrochemical passivation behavior of Sn-alloyed steel in chloride-containing media, which provides a preliminary theoretical basis for the composition design in this work, while the corrosion-wear performance of Sn-microalloyed wear-resistant steel is still unreported.

To fill the above research gaps, two types of Sn-microalloyed low-alloy wear-resistant steels were designed in this paper. The effects of Sn element on the continuous cooling transformation (CCT) behavior, microstructure and mechanical properties under different heat treatment processes, and corrosion-wear performance in chloride ion environments were systematically investigated. The regulation mechanism of Sn on the microstructure and service performance of low-alloy wear-resistant steel was revealed, and the optimal composition and heat treatment process scheme was determined. The research results can provide a theoretical basis and technical support for the composition design and performance optimization of low-alloy wear-resistant steel, and the developed steel can be applied to the core transmission components of archery training robots and other mechanical equipment under reciprocating friction and corrosive environments.

2. Engineering Application Background and Service Condition Analysis

The Sn-microalloyed low-alloy wear-resistant steel developed in this study is specifically designed for three types of core transmission wear-resistant components of the cable-driven archery training robot, namely the rope winding drum, guide pulley shaft, and transmission shaft. The functions and existing failure problems of each component are described as follows:

- Rope winding drum: As the core load-bearing component for steel cable winding and releasing, the surface rope groove is in long-term reciprocating sliding contact with the steel cable, making it the most severely

https://doi.org/10.64486/m.66.1.12

worn component. Currently, such components are mostly manufactured from conventional NM450 wear-resistant steel. In high-humidity training environments containing chloride ions, the rope groove is prone to corrosion-wear coupling failure, which reduces the groove profile accuracy, causes cable deviation, and impairs the positioning accuracy of the training target. Typically, the drum needs to be replaced within 1–2 years of service.

- Guide pulley shaft: It undertakes the steering and guiding function of the steel cable. The shaft surface is in continuous frictional contact with the inner ring of the pulley and the edge of the steel cable. Meanwhile, exposed to the outdoor environment, it is prone to wear-induced out-of-roundness, corrosion-induced seizure and other problems, and is a high-frequency maintenance component of the equipment.
- Transmission shaft: It serves as the power transmission component, bearing alternating bending torque and impact load during operation. Meanwhile, corrosive media can easily penetrate through the shaft end seal, resulting in corrosion fatigue fracture risk. Therefore, it imposes high requirements on both the strength-toughness and corrosion resistance of the material.

The low-alloy wear-resistant steel developed in this study is mainly oriented to the core transmission components of cable-driven archery training robots, including rope winding drums, drive shafts and guide pulley shaft systems. The overall structure of the archery training robot is composed of a drive device, pulleys, steel wire ropes, a training target and a column bracket. The drive device is the power core of the robot, which realizes the reciprocating motion of the target through the winding and releasing of the steel wire rope by the rope winding drum.

According to the actual service parameters of the equipment, the core transmission components are subjected to the following quantitative service conditions:

- Tribological load conditions: The rope winding drum is in long-term contact with the steel wire rope, with a contact stress of 200–400 MPa, a reciprocating motion frequency of 0.2–1 Hz, and a linear speed of 0.2–1.5 m/s; the drive shaft bears a torque of 50–150 N·m and an alternating bending load during operation.
- Corrosive environment conditions: The equipment is used in indoor and outdoor training venues, facing high humidity (relative humidity 60 %–95 %), chloride ions from athletes' sweat, and salt spray in coastal outdoor venues. The corrosive environment is simulated by 3.5 wt.% NaCl solution in this study.
- Performance requirements: The material is required to have a hardness ≥ 450 HV, yield strength ≥ 1100 MPa, and excellent low-temperature impact toughness to avoid brittle fracture; meanwhile, it must have good corrosion resistance and corrosion-wear resistance to ensure a service life of more than 5 years under the above working conditions.

3. Experimental Materials and Methods

3.1. Design of Experimental Materials

To address the comprehensive performance requirements of strength, toughness, wear resistance and corrosion resistance for the core components of archery training robots, two low-alloy wear-resistant steels with different Sn mass fractions were designed based on commercial NM450 wear-resistant steel (chemical composition listed in Table 1), designated as 0.03Sn steel and 0.20Sn steel, respectively. The experimental steels were smelted in a vacuum induction furnace, cast into 50 kg ingots, and then forged into billets with a cross-sectional dimension of 100 mm × 100 mm. Their chemical compositions are presented in Table 2.

Table 1. Chemical composition of the NM450

Steel	C / %	Si / %	Mn / %	Ni / %	Cr / %	P / %	S / %	Fe / %
NM450	0.26	0.70	1.10–1.60	0.80	0.40–1.5	0.025	0.01	Bal.

https://doi.org/10.64486/m.66.1.12

Table 2. Chemical composition of the experimental steels

Steel	C / %	Si / %	Mn / %	Sn / %	Cr / %	Fe / %
0.03Sn	0.15	0.55	0.45	0.042	1.01	Bal.
0.20Sn	0.16	0.40	0.30	0.20	1.00	Bal.

3.2. Experimental Methods

3.2.1. Continuous Cooling Transformation Test

The phase transformation temperatures of the experimental steels were determined using a Formastor-F II fully automatic dilatometer. Specimens with dimensions of Φ3 mm × 10 mm were machined from the quarter-thickness position of the forged billets, and a central hole of Φ2 mm × 2 mm was drilled at one end of each specimen to accommodate a thermocouple.

The critical points Ac_1 and Ac_3 were measured via a staged heating procedure: specimens were first heated to 500 °C at 10 °C/s, then to 900 °C at 0.05 °C/s, held at 900 °C for 3 min to ensure complete austenitization, and finally cooled to room temperature at 60 °C/s.

To further investigate the effect of cooling rate on microstructure, static continuous cooling transformation (CCT) curves were constructed. The phase transformation start and finish temperatures at different cooling rates were determined by the tangent method. Specimens were subjected to an identical austenitization treatment (heated to 900 °C at 10 °C/s, held for 3 min) followed by cooling to room temperature at rates of 0.5, 1, 2, 5, 10, 20, 40, and 60 °C/s.

After dilatometry testing, specimens were sectioned along the central axis to expose the region adjacent to the thermocouple. The sectioned samples were mechanically ground, polished, and etched with 4 vol.% nital solution. Microstructural characterization was performed using an optical microscope (OM) to identify the phase constituents formed at different cooling rates. Macrohardness measurements were conducted on a Future-Tech FM-700 hardness tester. The hardenability and phase transformation critical parameters measured in this experiment correspond to the actual quenching process window of large-size drum and shaft components of the robot, which can ensure that the whole cross-section of the components obtains a full martensitic structure under industrial mass production conditions and meet the process requirements of actual heat treatment.

3.2.2. Design of Heat Treatment Process

The forged billets were first subjected to hot rolling: heated to 1200 °C and held for 2 h, then hot-rolled through 7 passes to 12 mm thick plates. The rough rolling temperature was controlled at 1000–1100 °C, and the finish rolling temperature at 860~880 °C, followed by air cooling to room temperature.

Based on the phase transformation critical point test results, a quenching-tempering heat treatment process was designed: quenching temperatures were set at 870, 900, 930, and 960 °C, held for 15 min and then water-quenched. On the basis of the optimal quenching temperature, tempering temperatures were set at 160, 200, 240, and 280 °C, held for 40 min and then air-cooled. The regulation effect of heat treatment process on the microstructure and mechanical properties of the experimental steels was investigated. This study selects the quenching + low-temperature tempering process route, which matches the comprehensive requirements of high strength, high hardness and sufficient toughness for core transmission components, and directly corresponds to the service stress form of reciprocating impact + sliding wear borne by the components. It ensures that the microstructure state of the material after heat treatment adapts to the service load characteristics.

3.2.3. Microstructural Observation and Mechanical Property Testing

Metallographic samples were ground with 80# to 1500# sandpaper, polished with diamond paste, and etched with 4% (volume fraction) nitric acid alcohol solution. The microstructure was observed using a ZEISS ULTRA 55 field emission scanning electron microscope (FE-SEM). Macrohardness was tested with a KB300BVRZ-SA hardness tester under a load of 10 kg, and the average value of 8 test points was taken as the final result.

https://doi.org/10.64486/m.66.1.12

Bar-shaped tensile samples were prepared according to GB/T 228.1–2010 with a gauge length of 25 mm. Room-temperature tensile tests were performed on an AG-XPLUS 100 kN universal testing machine at a tensile rate of 1 mm/min. -40 °C low-temperature impact toughness was tested using a ZBC2452-B pendulum impact tester, with 3 parallel samples per group.

3.2.4. Immersion Corrosion and Corrosion-Wear Tests

A 3.5 wt.% NaCl solution was used to simulate the high-humidity and high-salt-spray corrosive environment of archery training robots. Immersion samples of 40 mm × 20 mm × 3 mm were prepared according to GB/T 19746-2018, with 3 parallel samples per group and immersion periods of 7, 14, 21, and 28 d. After immersion, the surface rust layer was removed by chemical derusting (500 mL HCl + 20 g urotropine + 500 mL H_2O). Mass changes before and after corrosion were measured with a precision electronic balance (accuracy 0.1 mg) to calculate mass loss. The parameter settings of this experiment are highly consistent with the actual service conditions of the target components.

Immersion corrosion test: The 28-day full immersion period is an accelerated corrosion equivalent duration, which can reflect the long-term rust layer evolution law of materials in outdoor service and verify the long-term corrosion resistance stability of components in high-humidity salt spray environments.

Corrosion-wear test: The ball-on-disc reciprocating contact mode is adopted to directly simulate the reciprocating sliding contact form between the rope winding drum, pulley shaft and the steel cable. The normal loads of 20 N, 30 N and 40 N correspond to the actual contact stress ranges of 200 MPa, 300 MPa and 400 MPa respectively. The 3.5 wt.% NaCl medium simulates the coupled corrosion environment of sweat and salt spray. The reciprocating motion mode is consistent with the working form of the components, which can truly reproduce the corrosion-wear synergistic failure mechanism in the service process, and the experimental results have clear engineering reference value.

A MFT 5000 friction and wear tester was used to simulate the reciprocating motion of the archery robot in a ball-on-disc reciprocating contact mode. The counterbody was a Φ6 mm Al_2O_3 ceramic ball, with normal loads of 20, 30, and 40 N, a reciprocating stroke of 5 mm, and a test duration of 120 min. The corrosive medium was 3.5 wt.% NaCl solution; meanwhile, the pure wear performance of the experimental steels was tested in deionized water using cathodic protection. After the test, the wear volume was measured with the built-in 3D surface profiler of the equipment.

4. Results and Discussion

4.1. Effect of Sn Element on Continuous Cooling Transformation Behavior

The microstructure of 0.03Sn steel under different cooling rates is shown in Figure 1. At a cooling rate of 0.5 °C/s, the steel is composed of ferrite and pearlite, with a high ferrite content and banded pearlite distributed around the ferrite matrix. As the cooling rate increases to 1 °C/s, the microstructure remains dominated by ferrite and pearlite, but the increased phase transformation driving force raises the nucleation rate, resulting in grain refinement and scattered pearlite distribution around ferrite grains. At low cooling rates, sufficient atomic diffusion and low phase transformation driving force lead to a high ferrite content.

When the cooling rate increases to 5 °C/s, bainite appears in the steel, and the ferrite content decreases significantly, with the microstructure consisting of ferrite, pearlite, and bainite. Bainite transformation is a medium-temperature transformation, forming a mechanical mixture of ferrite and carbides. Carbide precipitation occurs as carbon diffuses in ferrite, realizing a diffusive and coherent transformation. At 20 °C/s, the microstructure is mainly composed of martensite and a small amount of bainite. At this high cooling rate, atomic diffusion is inhibited, and atoms cannot complete phase transformation in the high-temperature austenite region before the temperature drops. Martensite transformation involves collective short-range migration of atoms, with an extremely fast growth rate after nucleation even at extremely low temperatures, resulting in diffusionless transformation when the temperature drops below the martensite start temperature.

https://doi.org/10.64486/m.66.1.12

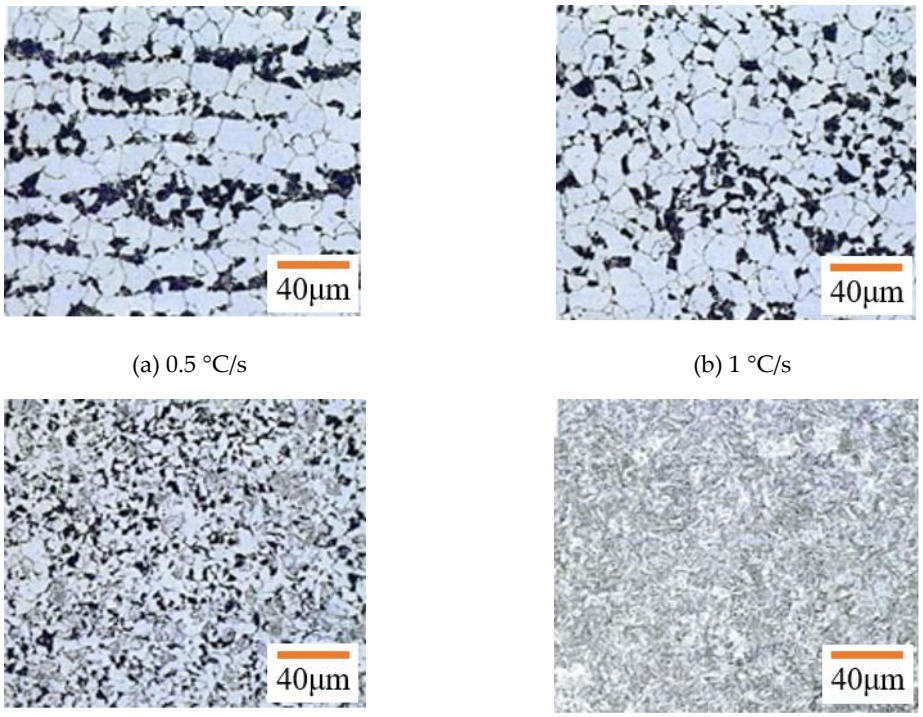

(a) 0.5 °C/s (b) 1 °C/s

(c) 5 °C/s (d) 20 °C/s

Figure 1. Microstructure of 0.03Sn steel under different cooling rates

The microstructure evolution of 0.20Sn steel under different cooling rates is shown in Figure 2. At 0.5 °C/s, the microstructure is ferrite and pearlite, with pearlite distributed in bands around ferrite. As the cooling rate increases to 5 °C/s, the microstructure changes significantly with the formation of bainite, consisting of ferrite, bainite, and a small amount of pearlite. At 20 °C/s, the microstructure is mainly martensite, bainite, and a small amount of ferrite. When the cooling rate increases to 40 °C/s, the microstructure is fully martensitic.

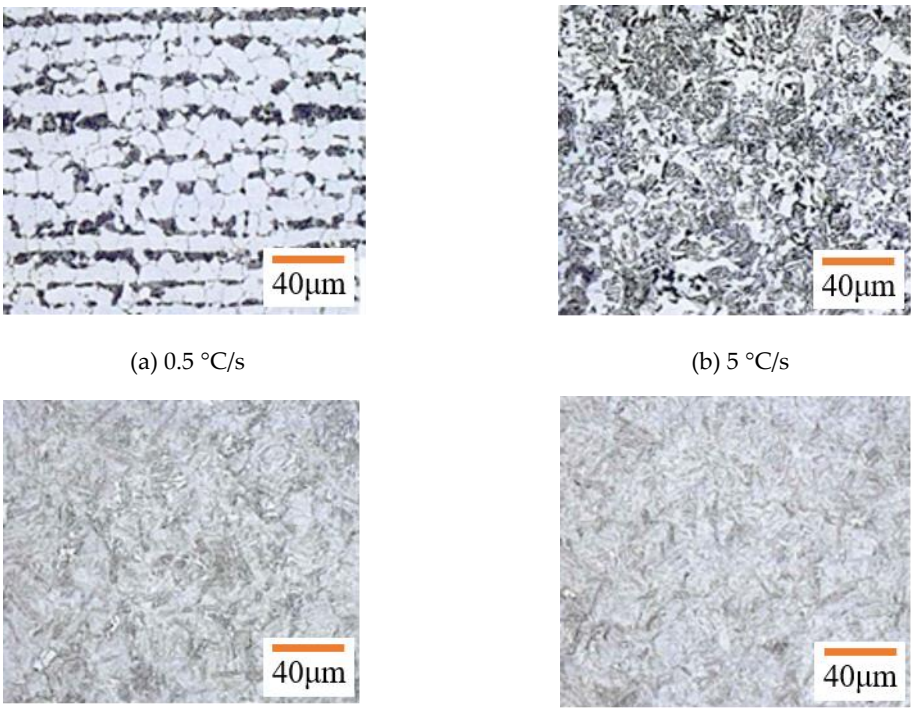

(a) 0.5 °C/s (b) 5 °C/s

(c) 20 °C/s (d) 40 °C/s

Figure 2. Microstructure of 0.20Sn steel under different cooling rates

https://doi.org/10.64486/m.66.1.12

The macrohardness of the two experimental steels as a function of cooling rate is shown in Figure 3. At low cooling rates (0.5–2) °C/s, the microstructure of 0.03Sn steel is dominated by ferrite and pearlite, resulting in good plasticity and toughness but low strength and hardness. When the cooling rate increases to 5 °C/s, the formation of bainite significantly increases the hardness. With further increases in cooling rate, the content of bainite and martensite increases, leading to a continuous rise in macrohardness. When the cooling rate exceeds 20 °C/s, the microstructure is fully martensitic, and the macrohardness increases slowly.

At the same cooling rate, the macrohardness of 0.20Sn steel is slightly lower than that of 0.03Sn steel, which is related to the slight segregation of Sn at grain boundaries. However, the hardness level of both steels meets the wear resistance requirements of the core components of the robot.

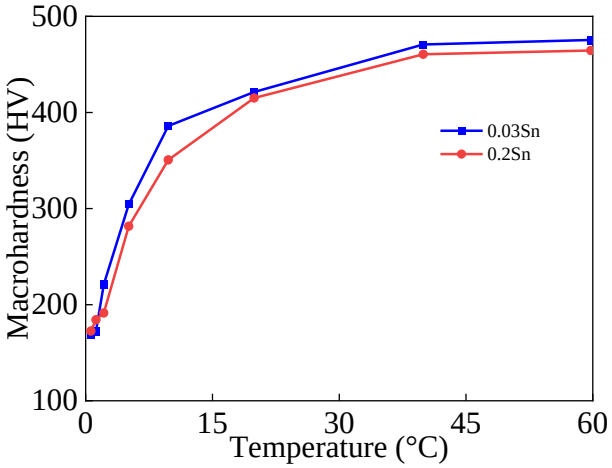

Figure 3. Macrohardness of experimental steels under different cooling rates

In this study, the thermal dilatometry method was employed. Ferrous materials are substances that undergo polymorphic phase transformations. When heated to a certain temperature, the high-temperature phase and its transformation products upon cooling have different crystal structures, which alters the linear relationship between dilation and temperature. As shown in Fig. 4, the point where the dilation-time curve begins to deviate from the linear growth segment is defined as the onset point of phase transformation. When the phase transformation is complete, the phase composition of the specimen stabilizes, and the dimensional change with temperature returns to linearity; the point where the curve regains linearity is regarded as the completion point of phase transformation. The tangent method was used to determine the phase transformation temperatures of the two experimental steels. The Ac_1 and Ac_3 temperatures of the 0.042Sn experimental steel were 724 °C and 830 °C, respectively, while those of the 0.2Sn experimental steel were 738 °C and 841 °C, respectively.

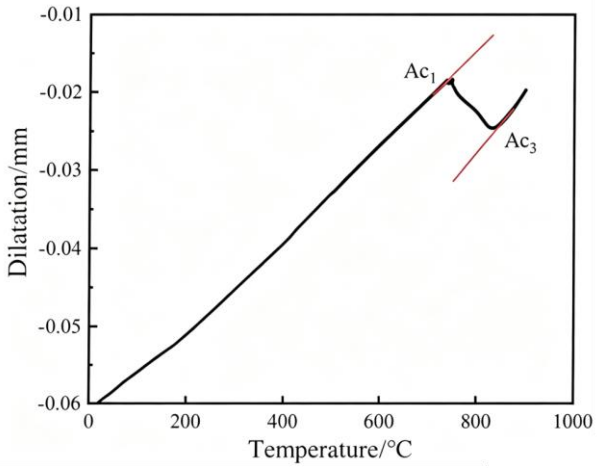

Figure 4. Thermal expansion curve of experimental steel

https://doi.org/10.64486/m.66.1.12

4.2. Effect of Quenching and Tempering Temperatures on Microstructure and Mechanical Properties

The mechanical properties of 0.03Sn steel after quenching at different temperatures are shown in Table 3. The elongation reaches a maximum of 11.3% at 960 °C. For low-alloy wear-resistant steel, wear resistance is closely related to hardness: when the matrix structure is the same, wear resistance has a linear relationship with hardness; under the same hardness condition, better plasticity and toughness result in higher wear resistance.

Table 3. Mechanical properties of 0.03Sn steel after quenching at different temperatures

Temperature °C	Hardness HV	- 40 ℃ Impact Energy / J	Yield Strength MPa	Tensile Strength MPa	Elongation %
870	471	89.4	1170	1404	9.7
900	469	97.0	1163	1402	10.5
930	471	73.2	1141	1406	10.9
960	467	55.3	1140	1418	11.3

The macrohardness curve of 0.03Sn steel is shown in Figure 5. The macrohardness is 471 HV at 870 °C, 469 HV at 900 °C, and 467 HV at 960 °C. Since the microstructure is martensitic at all quenching temperatures, the hardness variation is small. The -40 °C impact energy of 0.03Sn steel is 89.4 J at 870 °C, reaches a maximum of 97.0 J at 900 °C, and decreases significantly to 55.3 J at 960 °C. Comprehensive comparison shows that 0.03Sn steel achieves the best overall mechanical properties when quenched at 900 °C.

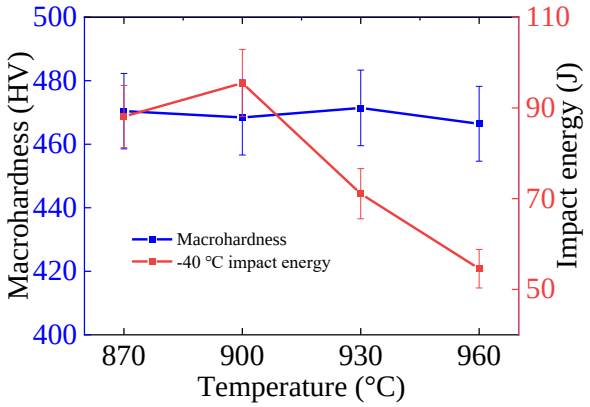

Figure 5. Mechanical properties of 0.03Sn steel after quenching at different temperatures

The macrohardness of 0.20Sn steel after quenching at different temperatures is shown in Figure 6. The maximum macrohardness of 466 HV is achieved at 900 °C, and it decreases to 459 HV at 960 °C. The -40 °C impact energy of 0.20Sn steel increases slightly with quenching temperature, from 48.86 J at 900 °C to 54.3 J at 960 °C, with a slow upward trend. Comprehensive mechanical properties show that 0.20Sn steel exhibits the best overall performance when quenched at 900 °C.

Table 4. Mechanical properties of 0.20Sn steel after quenching at different temperatures

Temperature °C	Hardness HV	- 40 °C Impact Energy / J	Yield Strength MPa	Tensile Strength / MPa	Elongation / %
870	465	46.61	1108	1387	12.16
900	466	48.86	1121	1395	12.23
930	463	52.73	1090	1371	11.92
960	459	54.30	1086	1363	12.12

https://doi.org/10.64486/m.66.1.12

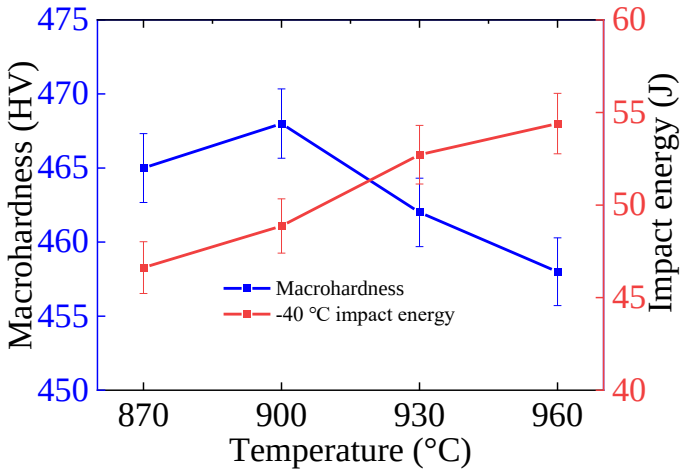

Figure 6. Mechanical properties of 0.20Sn steel after quenching at different temperatures

Based on the optimization results of quenching temperature, 900 °C was selected as the optimal quenching temperature to study the effect of tempering temperature on mechanical properties. With increasing tempering temperature, the hardness and strength of both steels show a slow downward trend, while toughness remains stable initially and then decreases significantly. 0.03Sn steel achieves the best overall performance at 160 °C tempering, with an impact energy of 98 J and hardness of 468 HV. 0.20Sn steel exhibits optimal performance at 200 °C tempering, with an impact energy of 49 J and hardness of 448 HV. When the tempering temperature exceeds 200 °C, increased segregation of Sn at grain boundaries leads to a significant decrease in impact toughness. Therefore, the optimal heat treatment processes are determined as follows: 0.03Sn steel: 900 °C quenching + 160 °C tempering; 0.20Sn steel: 900 °C quenching + 200 °C tempering. Combined with the service performance requirements, it can be seen that after the optimal heat treatment, both experimental steels have a hardness higher than 450 HV and a yield strength higher than 1100 MPa, which fully meet the strength and hardness access requirements of the core transmission components of the archery training robot.

4.3. Corrosion and Wear Behavior

The corrosion mass loss of the two experimental steels after immersion in 3.5 wt.% NaCl solution for different periods is shown in Figure 7. The mass loss increases with immersion time, and the mass loss of 0.20Sn steel is consistently lower than that of 0.03Sn steel in all test periods. After 28 d of immersion, the mass loss of 0.03Sn steel is significantly higher than that of 0.20Sn steel, indicating that the rust layer of 0.20Sn steel provides better protection for the matrix against external erosion, reducing material loss with extended corrosion time.

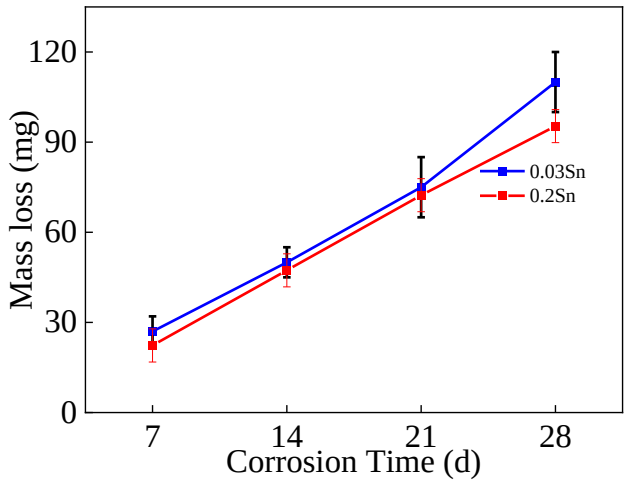

Figure 7. Mass loss of experimental steels during different corrosion periods

https://doi.org/10.64486/m.66.1.12

To conduct a more detailed analysis of the thickness variation of rust layers on experimental steels after immersion corrosion for different durations, the cross-sectional thicknesses of rust layers on the two experimental steels were characterized, and the results are presented in Fig. 8. As shown in Fig. 8(a) and (b), a thin rust layer formed on the surface of the steel matrix after immersion in 3.5 wt.% NaCl solution for 7 days. After 14 days of immersion, the rust layers of the experimental steels exhibited a two-layer structure: the region marked by yellow dashed lines in Fig. 8(c) and (d) corresponds to the inner rust layer, which is connected to the steel matrix and relatively dense; the region marked by blue dashed lines corresponds to the outer rust layer, which is in direct contact with the external environment and relatively loose and porous. Morphological observations revealed that pores and cracks existed in the outer rust layer, while the inner rust layer was more uniform and dense than the outer rust layer and exhibited stronger adhesion to the steel matrix.

During the corrosion process, mass exchange occurs through three interfaces: outer rust layer–air, outer rust layer–inner rust layer, and inner rust layer–matrix. Dissolved oxygen is present in the solution during the corrosion reaction, which reacts with Fe atoms. Specifically, Fe atoms dissolve at the surface of the experimental steels to form the outer rust layer, which is mainly composed of γ-FeOOH. The outer rust layer has weak adhesion to the matrix and contains numerous pores, allowing the penetration of Cl^- and other aggressive species. Subsequently, corrosion-resistant elements participate in the formation of the inner rust layer at the interface between the outer rust layer and the matrix, resulting in the formation of amorphous spinel-type oxides, amorphous stable FeOOH inner rust layers, or cation-selective rust layers. These layers can effectively block the penetration of aggressive ions, thereby retarding the corrosion process and improving the corrosion resistance of the experimental steels.

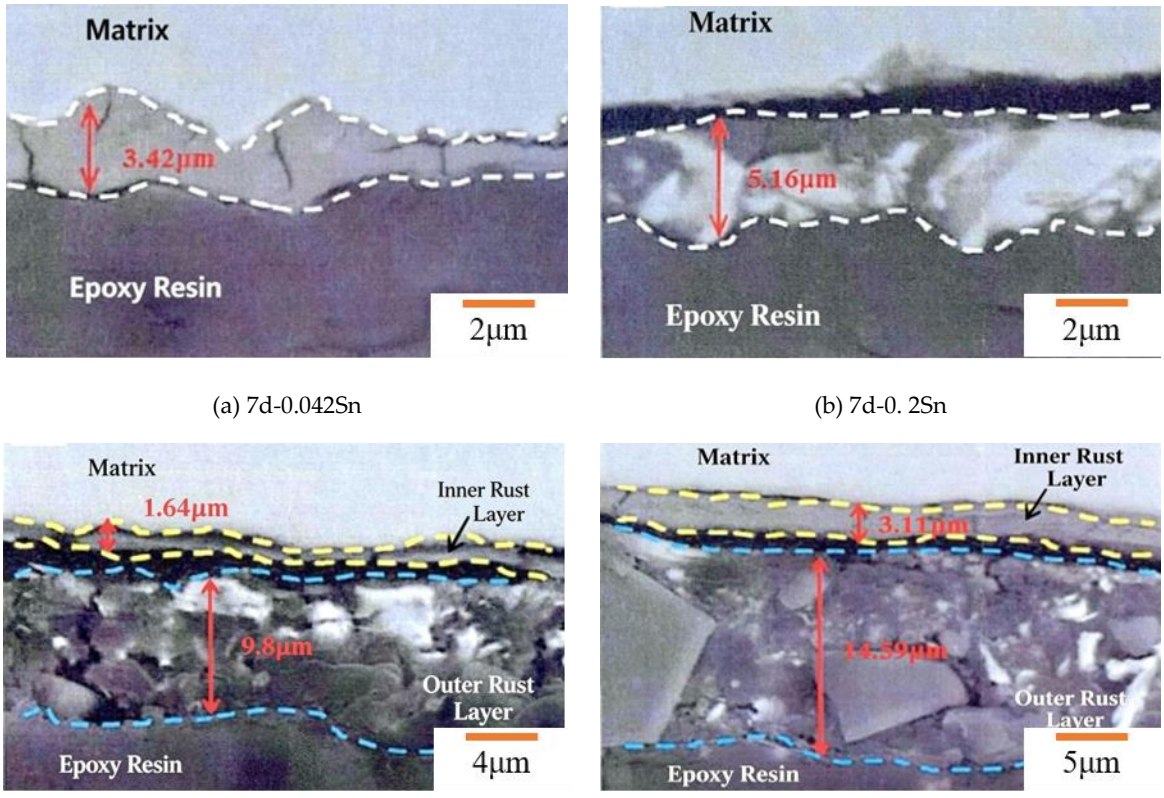

(a) 7d-0.042Sn (b) 7d-0. 2Sn

(c) 14d-0.042Sn (d) 14d-0. 2Sn

Figure 8. Microscopic morphologies of sections of experimental steel with different corrosion cycles

The total corrosion-wear volume of the experimental steels in 3.5 wt.% NaCl solution is shown in Figure 9. At a load of 20 N, NM450 steel has the largest volume loss of 5.87×10^{-3} mm³, followed by 0.03Sn steel (5.31×10^{-3} mm³), and 0.20Sn steel exhibits the best corrosion-wear resistance with a volume loss of 4.65×10^{-3} mm³.

https://doi.org/10.64486/m.66.1.12

As the load increases, the wear volume of all three steels increases significantly. At 40 N, the wear volume of NM450 steel is 19.7×10⁻³ mm³, 0.03Sn steel is 15.07×10⁻³ mm³, and 0.20Sn steel is the smallest at 11.3×10⁻³ mm³. At 40 N, the wear volume of NM450 steel is 1.69 times that of 0.20Sn steel. The increase in wear volume with load is attributed to the deeper indentation of micro-protrusions on the friction surface into the matrix under higher external forces, which increases the friction between the counterbody and the matrix, generates larger shear stress, and leads to more material loss during friction. The corrosion and corrosion-wear results show that 0.20Sn steel can specifically solve the core pain point of "corrosion-wear synergistic failure" of archery training robot components. The dense inner rust layer induced by Sn can resist the erosion of sweat and salt spray and reduce the weakening effect of corrosion on the matrix.

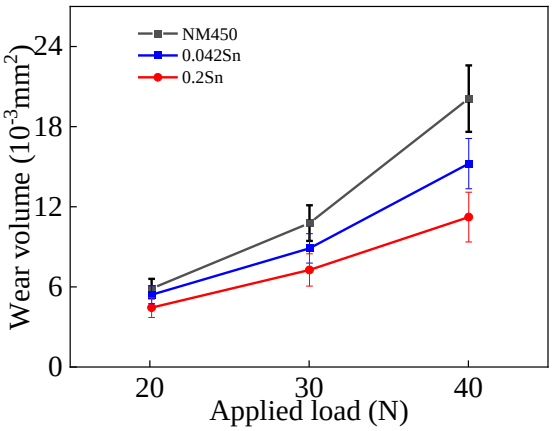

Figure 9. Corrosion-wear volume of experimental steels in 3.5 wt.% NaCl solution

5. Conclusions

Two Sn-microalloyed low-alloy wear-resistant steels were designed in this paper. The effects of Sn element on the phase transformation behavior, heat treatment process, mechanical properties, corrosion resistance, and corrosion-wear performance of the experimental steels were systematically studied, and the main conclusions are as follows:

1. Sn element has no significant effect on the type of continuous cooling transformation of the experimental steels. Both 0.03Sn steel and 0.20Sn steel achieve full martensitic structure at a critical cooling rate of 20 °C/s, exhibiting excellent hardenability that meets the heat treatment requirements of core components of the robot.
2. The optimal quenching and tempering processes for the two experimental steels are determined as: 0.03Sn steel (900 °C quenching + 160 °C tempering) and 0.20Sn steel (900 °C quenching + 200 °C tempering). After the optimal heat treatment, 0.03Sn steel exhibits excellent toughness with a -40 °C impact energy of 98 J. 0.20Sn steel has comparable hardness and strength to 0.03Sn steel, and although its toughness is slightly lower, it still meets the service requirements of core components of the robot.
3. Sn element significantly enhances the corrosion resistance and corrosion-wear performance of the experimental steels. After 28 days of immersion in 3.5 wt.% NaCl solution, the mass loss of 0.20Sn steel is 37.8 % lower than that of 0.03Sn steel. Under the load of 40 N, the corrosion-wear volume of 0.20Sn steel is only 58.6 % of that of NM450 steel. The hardness, strength, low-temperature toughness and corrosion-wear performance of the experimental steels all meet the service performance requirements of the rope winding drum, guide pulley shaft and transmission shaft of the archery training robot. They can effectively alleviate the corrosion-wear synergistic failure problem, and significantly improve the service life of components and the operation stability of the equipment.

https://doi.org/10.64486/m.66.1.12

References

1. X. Xu, W. Xu, F. H. Ederveen, et al., "Design of low hardness abrasion resistant steels," *Wear*, vol. 301, no. 1-2, pp. 89–93, 2013. https://doi.org/10.1016/j.wear.2013.01.002
2. Z. Y. Ma, J. Fang, and Y. T. Yang, "Properties improvement of low alloy wear resistant steel casting for coal-mining machinery," *Chinese Journal of Mechanical Engineering*, vol. 24, no. 1, pp. 78–82, 2011. https://doi.org/10.3901/CJME.2011.01.078
3. D. Wu, H. Zhang, S. Liu, et al., "Effect of microstructure on wear resistance of low-alloy high-strength wear-resistant steel," *International Journal of Electrochemical Science*, vol. 14, no. 8, pp. 7570–7581, 2019. https://doi.org/10.20964/2019.08.20
4. X. Su, G. Xu, M. Zhu, et al., "Investigation on the interaction between corrosion and wear of U68CuCr rail steel with different corrosion periods," *Wear*, vols. 516-517, p. 204598, 2023. https://doi.org/10.1016/j.wear.2022.204598
5. T. Zirari and V. Trabadelo, "A review on wear, corrosion, and wear-corrosion synergy of high entropy alloys," *Heliyon*, vol. 10, no. 4, p. e25867, 2024. https://doi.org/10.1016/j.heliyon.2024.e25867
6. L. Sun, S. Zhang, R. Song, et al., "Effect of V, Nb, and Ti microalloying on low–temperature impact fracture behavior of non–quenched and tempered forged steel," *Materials Science and Engineering: A*, vol. 871, p. 145299, 2023. https://doi.org/10.1016/j.msea.2023.145299
7. Z. He, Y. Dong, Y. Tian, et al., "Effect of Cr content on the microstructure and corrosion resistance of laser cladded FeCoNiMnAl0.5Crx high entropy alloy coatings," *Journal of Alloys and Compounds*, vol. 1043, p. 184249, 2025. https://doi.org/10.1016/j.jallcom.2025.184249
8. J. Chen, Z. Shi, X. Luo, et al., "Micro-Alloying Effects on Microstructure and Weldability of High-Strength Low-Alloy Steel: A Review," *Materials*, vol. 18, no. 5, p. 1036, 2025. https://doi.org/10.3390/ma18051036
9. H. Luo, H. Su, B. Li, et al., "Electrochemical and passive behaviour of tin alloyed ferritic stainless steel in concrete environment," *Applied Surface Science*, vol. 439, pp. 232–239, 2018. https://doi.org/10.1016/j.apsusc.2017.12.243
10. C. Jiang, Y. Yang, X. Cheng, et al., "Effect of Sn on the corrosion behavior of weathering steel in a simulated tropical marine atmosphere," *Anti-Corrosion Methods and Materials*, vol. 67, no. 2, pp. 129–139, 2020. https://doi.org/10.1108/ACMM-09-2019-2178
11. W. Zhuang-Fei, T. Shuai, L. Zhen-Yu, et al., "Effect of Nb on Continuous Cooling Transformation Behavior of Low Carbon Microalloyed Steel," *Journal of Northeastern University (Natural Science)*, vol. 35, no. 8, pp. 1097–1101, 2014. https://doi.org/10.3969/j.issn.1005-3026.2014.08.012
12. S. I. Teraoka and A. Seki, "Effects of Grain Boundary Segregation of Sn and P on Toughness of Ultra Low Carbon Ferritic Stainless Steels," *Tetsu-to-Hagane*, vol. 107, no. 8, pp. 661–671, 2021. https://doi.org/10.2355/tetsutohagane.tetsu-2020-126
13. J. J. Shi and J. Ming, "Influence of mill scale and rust layer on the corrosion resistance of low-alloy steel in simulated concrete pore solution," *International Journal of Minerals, Metallurgy and Materials*, vol. 24, no. 11, pp. 1270–1279, 2017. https://doi.org/10.1007/s12613-017-1379-4
14. M. Liu, C. Du, and J. L. X. Zhang, "Effect of nitrogen on the corrosion behavior of high-strength low-alloy steel in simulated marine atmosphere," *Journal of Materials Science*, vol. 58, no. 31, pp. 12827–12845, 2023. https://doi.org/10.1007/s10853-023-08802-y
15. H. Y. Wen, Y. Ma, L. B. Wang, et al., "Influence of heat treatment on microstructure and wear resistance of a medium-carbon-low-alloy wear-resistant steel," *Transactions of Materials and Heat Treatment*, vol. 32, no. 12, pp. 72–77, 2011. https://doi.org/10.1016/S1005-0302(11)60031-5
16. H. H. Wang and M. Du, "Corrosion Behavior of a Low-Carbon Steel in Simulated Marine Splash Zone," *Acta Metallurgica Sinica (English Letters)*, vol. 30, no. 10, pp. 1077–1086, 2017. https://doi.org/10.1007/s40195-017-0535-1
17. S. Zhang, "Effect of Tempering Temperature on the Corrosion Behavior of R5 Steel in Artificial Seawater," *International Journal of Electrochemical Science*, vol. 12, no. 3, pp. 2453–2465, 2017. https://doi.org/10.20964/2017.03.69
18. C. Liu, X. Cheng, Z. Dai, et al., "Synergistic Effect of Al_2O_3 Inclusion and Pearlite on the Localized Corrosion Evolution Process of Carbon Steel in Marine Environment," *Materials*, vol. 11, no. 11, p. 2277, 2018. https://doi.org/10.3390/ma11112277

https://doi.org/10.64486/m.66.1.12

19. Y. Zhang, J. Sun, H. Lei, et al., "Influence of citric acid passivation treatment on the marine atmospheric corrosion resistance of L80-13Cr stainless steel," *Discover Applied Sciences*, vol. 7, p. 226, 2025. https://doi.org/10.1007/s42452-025-06667-1
20. C. Fu, W. Yi, D. Y. Zhang, et al., "Electrochemical corrosion behavior of Sn-58Bi-XNi solder alloy in 3.5 wt.% NaCl solution," *Journal of Materials Science: Materials in Electronics*, vol. 36, p. 2266, 2025. https://doi.org/10.1007/s10854-025-16358-7

https://doi.org/10.64486/m.66.1.12